

An Intrinsically Glassy Metallic Coordination Polymer Showing Thermally and Aerobically Robust Conductivity

John Anderson (✉ jsanderson@uchicago.edu)

University of Chicago <https://orcid.org/0000-0002-0730-3018>

Jiaze Xie

University of Chicago

Simon Ewing

University of Chicago

Jan-Niklas Boyn

University of Chicago

Baorui Cheng

Alexander Filatov

University of Chicago <https://orcid.org/0000-0002-8378-1994>

Tengzhou Ma

University of Chicago

Norman Zhao

University of Chicago

Ram Itani

University of Chicago

Xiaotong Sun

University of Chicago

Himchan Cho

University of Chicago

Shrayesh Patel

University of Chicago

Dmitri Talapin

University of Chicago <https://orcid.org/0000-0002-6414-8587>

Jiwoong Park

University of Chicago <https://orcid.org/0000-0002-0511-1442>

David Mazziotti

University of Chicago <https://orcid.org/0000-0002-9938-3886>

Keywords:

Posted Date: February 2nd, 2022

DOI: <https://doi.org/10.21203/rs.3.rs-1281292/v1>

License:  This work is licensed under a Creative Commons Attribution 4.0 International License.

[Read Full License](#)

Version of Record: A version of this preprint was published at Nature on October 26th, 2022. See the published version at <https://doi.org/10.1038/s41586-022-05261-4>.

An Intrinsically Glassy Metallic Coordination Polymer Showing Thermally and Aerobically Robust Conductivity

Jiaze Xie, Simon Ewing, Jan-Niklas Boyn, Baorui Cheng, Alexander S. Filatov, Tengzhou Ma, Norman Zhao, Ram Itani, Xiaotong Sun, Himchan Cho, Shrayesh N. Patel, Dmitri V. Talapin, Jiwoong Park, David A. Mazziotti, and John S. Anderson*

Summary Paragraph

Conducting organic materials, such as doped organic polymers,¹ molecular conductors,^{2,3} and emerging coordination polymers,⁴ underpin technologies ranging from displays to flexible electronics.⁵ Realizing high electrical conductivity in traditionally insulating organic materials necessitates tuning their electronic structure through chemical doping.⁶ Furthermore, even materials that are intrinsically conductive, such as single-component molecular conductors,^{7,8} require crystallinity for metallic behavior. However, commercial conducting polymers are often purposefully amorphous to aid in durability and processability.^{9,10} Using molecular design to engender high conductivity in undoped amorphous materials would enable tunable and robust conductivity in many applications, but there are no intrinsically conducting organic materials which maintain high conductivity when disordered. Here we show that the completely amorphous coordination polymer Ni tetrathiafulvalene tetrathiolate (NiTTFtt) displays intrinsic metallic conductivity. Despite its disordered structure, NiTTFtt exhibits remarkably high electronic conductivity (1280 S/cm) and intrinsically glassy metallic behavior. Analysis with advanced theory shows that these properties are enabled by strong molecular overlap and correlation that are robust to structural perturbations. This unusual set of structural and electronic features results in remarkably stable organic conductivity which is maintained in air for weeks and at temperatures up to 140 °C. Our results demonstrate that molecular design can enable metallic conductivity even in heavily disordered materials. This both raises fundamental questions about how band-like transport can exist in the absence of periodic structure as well as suggests exciting new applications for these materials.

Introduction

Using molecular design to engender high conductivity in undoped amorphous materials would enable tunable and robust conductivity in many applications, but there are no intrinsically conducting organic materials which maintain high conductivity when completely disordered. Inorganic glassy metals have been discovered but require careful fabrication.¹¹ Furthermore, the relationship between metallic behavior, which classically requires periodicity giving rise to a well-defined band structure, and geometric disorder in these materials is still unclear.¹² Electron-rich and redox-active tetrathiafulvalene (TTF) motifs feature prominently as molecular building blocks in conducting materials.⁸ Appending thiolate groups to TTF to generate tetrathiafulvalene-tetrathiolate (TTFtt) enables the formation of extended coordination polymers that combine the properties of TTF with the rich electronic structures of transition metal dithiolenes.¹³ While the promise of these materials has been recognized, their structure, purity, composition, and hence properties are not well-defined due to synthetic challenges.¹⁴

We recently discovered syntheses that enable the isolation of a series of redox congeners of capped TTFtt compounds and their facile transmetalation to group 10 metals.¹⁵ Here we report that this synthetic strategy enables the isolation of the material NiTTFtt in high purity as an amorphous powder. Despite its disordered structure, NiTTFtt exhibits remarkably high conductivity of 1280 S/cm (room temperature, four-probe measurement) and intrinsically glassy metallic behavior. Advanced theoretical analysis shows that these properties are enabled by strong molecular overlap and correlation that are robust to structural perturbations. This unusual set of structural and electronic features results in remarkably stable conductivity which is maintained in air for weeks and at temperatures up to 140 °C. The unusual properties of NiTTFtt demonstrate that molecular design can enable metallic conductivity even in completely disordered materials. This finding raises fundamental questions about charge transport mechanisms in disordered materials and suggests exciting new applications for intrinsically metallic organic materials.

Synthesis and Structure

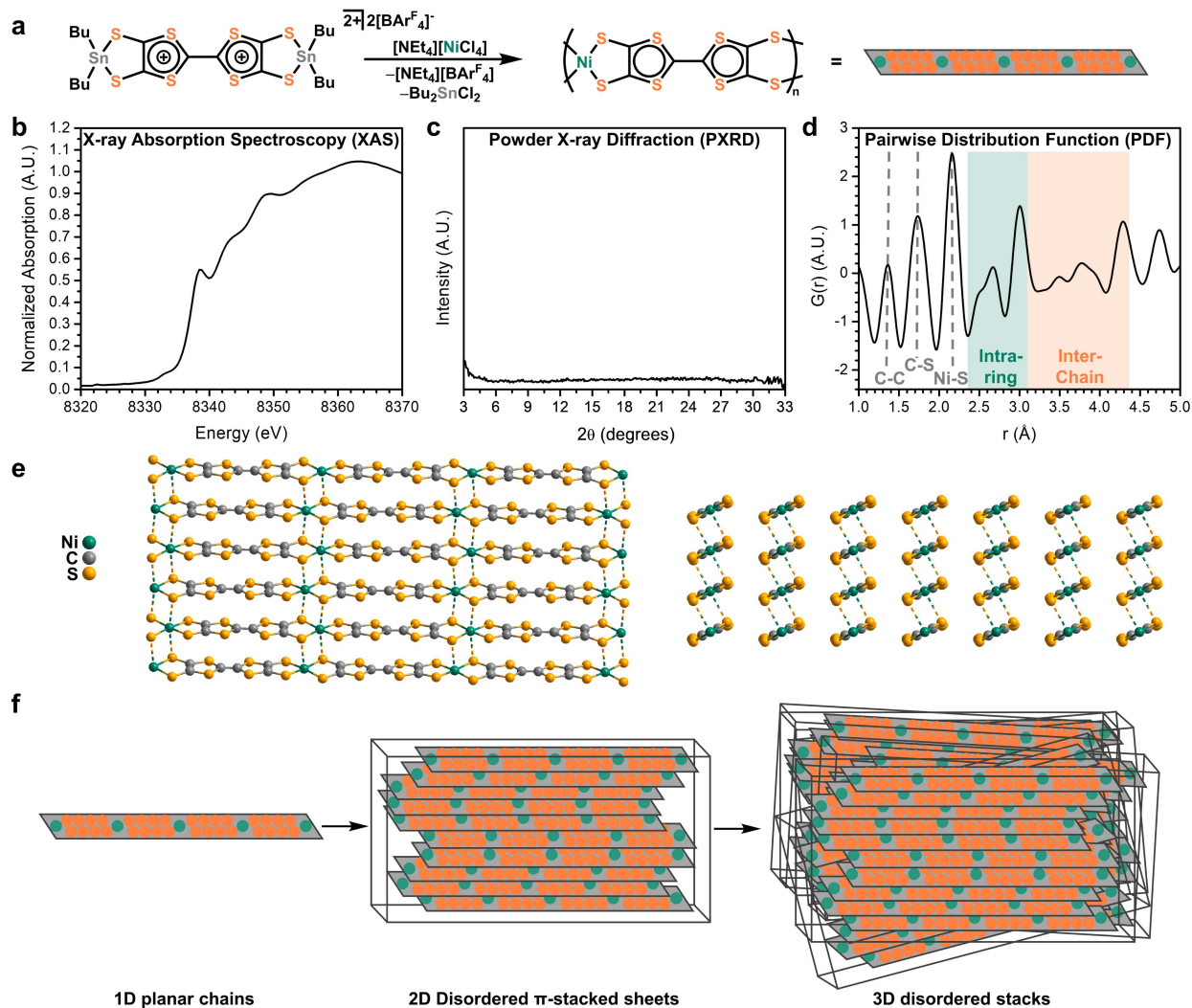


Fig. 1 Synthesis and structure of NiTTFtt. **a**, Synthetic scheme. **b**, PXRD data. **c**, PDF data. **d**, XAS spectrum. **e**, Modeled structure. **f**, Hierarchical structure showing molecularly ordered chains but disordered packing in sheets and stacks.

NiTTFTt is synthesized by mixing [TTFtt(SnBu₂)₂][BAR^F₄]₂ (BAR^F₄ = tetrakis(3,5-bis(trifluoromethyl)phenyl)borate) with excess [TEA]₂[NiCl₄] (Fig. 1a, TEA = tetraethylammonium). The composition of NiTTFTt was verified by several techniques which all support a Ni:S ratio of 1:8 (Table S2). Combustion analysis confirms the proposed formula of NiTTFTt with [Bu₂Sn][BAR^F] chain terminations. The absence of any ammonium counterions implies that the TTF cores have formal 2+ charges which is also supported by the absence of Electron Paramagnetic Resonance signals (Fig. S17).⁸ X-ray photoelectron spectroscopy (Fig. S13 and S14) reveals peaks at 871 and 854 eV, which can be assigned as Ni 2p_{1/2} and 2p_{3/2} peaks respectively, and a satellite at 860 eV associated with a plasmon loss, all of which are consistent with low-spin (*S* = 0) square planar Ni(II) centers. The S 2p spectra appear as head and shoulder patterns spanning 161-166 eV suggesting the existence of multiple sulfur sites in NiTTFTt similar to spectra of TTF[Nidmit₂] (dmit, 1,3-dithole-2-thione-4,5-dithiolate).¹⁶ Ni K-edge X-ray absorption spectroscopy shows an intense rising edge at 8338.6 eV which also supports the assignment of square planar Ni(II) centers (Fig. 1b).¹⁷

Powder X-ray diffraction (PXRD) data was also collected (Fig. 1c). There are no apparent features in the PXRD pattern for NiTTFTt, suggesting that this material is completely amorphous with domain sizes < 1 nm.¹⁸ Therefore, we have investigated the structure of NiTTFTt with pairwise distribution function (PDF) analysis (Fig. 1d). The peaks below 3 Å can be assigned to C–C, C–S, and Ni–S bonds and intraring distances. The peaks between 3-4.5 Å represent interchain distances and are consistent with typical intermolecular S–S distances in TTF systems. Notably, the peaks in this region are broader, suggesting that the interchain interactions in NiTTFTt are irregular, consistent with its amorphous structure.

Despite the amorphous nature of NiTTFTt, we have built a structural model based on experimental data (Fig. 1e). This model is supported by attempts to grow more crystalline NiTTFTt by slow diffusion which shows a PXRD pattern that can be indexed to a monoclinic unit cell (Fig. S6, S11, S12). This unit cell constrains the model to staggered chain packing and the PDF data suggests S–S distances of ~3.4-3.7 Å along the π -stack and ~3 and 4 Å side-to-side between chains (Fig. 1d, S9). These values are similar to those observed in the single-component molecular metal, [Ni(tmtd)₂] (tmtd, trimethylene-tetrathiafulvalene-dithiolate),¹⁹ and also support tight packing as previously proposed.²⁰ Based on this model, the disordered structure of NiTTFTt arises from 1D chains that pack face-to-face to generate disordered 2D sheets which then pack side-to-side to generate a 3D structure (Fig. 1f). Indeed, scanning electron microscopy (SEM) clearly reveals the presence of 2D flakes (Fig. S10).

Physical Properties

With this structural information on NiTTFTt we then turned to examine its electronic structure. Four-probe conductivity measurements on a hot pressed pellet of amorphous NiTTFTt reveal a remarkable room temperature conductivity of 1280 S/cm (Fig. 2a). This value is similar to the most conductive coordination polymer (Cu₃BHT, 2500 S/cm, BHT = benzenehexathiolate)²¹ even though Cu₃BHT is measured as a highly crystalline thin film while the pressed pellet of NiTTFTt has much higher contributions from grain boundaries. The thermal conductivity of NiTTFTt as measured by Raman thermometry (Fig. S22),²² is 6.3 W/mK which is similar to inorganic glassy metals,²³ but much higher than what is typical for coordination polymers (< 0.4 W/mK).²⁴ The

combination of high electrical and thermal conductivity suggests that electrons serve as carriers for both charge and thermal transport.

Variable temperature conductivity experiments on pressed pellets of amorphous NiTTFt were then undertaken (Fig. 2b). These measurements show an almost temperature-independent electrical resistivity with only a slight increase at low temperatures. Fitting this data with an Arrhenius plot indicates an activation energy of only 2.1 meV above 60 K and 0.08 meV below 20 K (Fig. S25).²¹ These extremely small barriers may arise for two reasons. Firstly, macroscopic grain boundaries may provide a barrier to charge flow as is frequently observed in pressed pellets of conducting organic materials.^{7,25} Alternatively, a flat conductivity profile with temperature has been observed for glassy metals which have resistivities greater than 150 $\mu\Omega/\text{cm}$.²⁶ The increase of resistivity as temperature decreases is proposed to arise from “weak localization” with a characteristic $T^{1/2}$ upturn in resistivity due to electron-electron interactions. We observe this same $T^{1/2}$ dependence at low temperature, suggesting similar behavior in NiTTFt. This observation, combined with the fact that extrapolation of the resistivity results in a finite zero-temperature limit, suggests that NiTTFt is best thought of as having metallic character.²⁶

Charge transport in disordered systems is typically analyzed with variable-range hopping models. Application of a 3D model to the resistivity data of NiTTFt reveals a $T_0 < 100$ K which indicates a high density of states at the Fermi level (Fig. S26). Ultraviolet photoelectron spectroscopy (UPS) conducted on a pellet of NiTTFt also supports a non-zero density of states at the Fermi level (Fig.

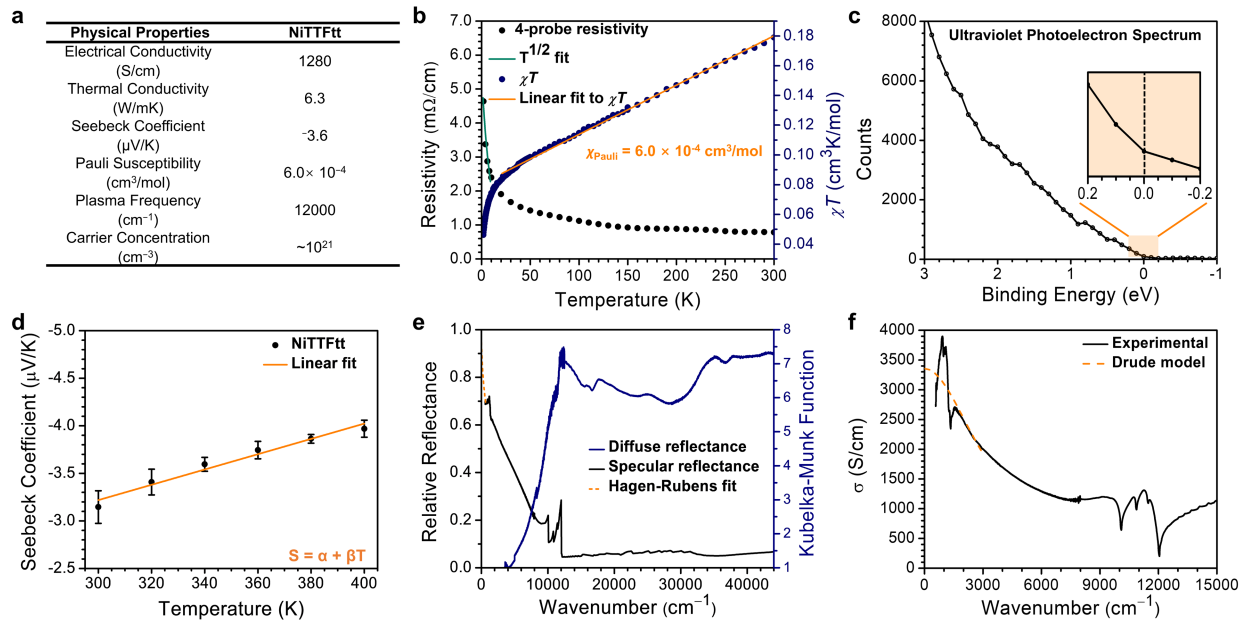


Fig. 2 Physical properties of NiTTFt. **a**, Summary of electronic, thermal, and magnetic properties. **b**, Variable temperature resistivity (black) and magnetic susceptibility (blue) data. The green line indicates a $T^{1/2}$ fit to the resistivity data at low temperature while the orange line indicates a linear fit to the magnetic susceptibility data with the shown Pauli paramagnetic contribution. **c**, Ultraviolet photoelectron spectrum showing a non-zero density of states at the Fermi level. **d**, Variable temperature Seebeck coefficient measurements showing a linear relationship (orange). **e**, Specular (black) and diffuse (blue) reflectance data. A Hagen-Rubens fit at low energy is shown as an orange dashed line. **f**, Optical conductivity at the low energy limit with a Drude model fit shown as an orange dashed line.

2c). Values of T_0 between $1-10^4$ K are commonly observed in granular metals and cermets where the model assumes hopping between metallic islands.²⁷ The observed $T^{1/2}$ upturn in resistivity led us to apply the Efros-Shklovskii model to the low temperature region. The observed linear relationship indicates the presence of a Coulomb gap which further suggests electron-electron interactions as discussed above. Interestingly, the T_{ES} value obtained from this fit is < 3 K, which is extremely small. Such a small value may suggest large delocalization lengths.²⁸ All these data support that NiTTFt is best described as a glassy metal.

We then pursued additional orthogonal measurements to verify metallic character in NiTTFt. The Seebeck coefficient (S) of NiTTFt is $-3.6 \mu\text{V/K}$ and the magnitude of this value increases in a linear fashion with temperature (Fig. 2d). The negative Seebeck coefficient suggests that electrons are the charge carriers in NiTTFt and the observed small magnitude and linear scaling with temperature are commonly observed in metallic inorganic conductors.²⁹ The magnetic susceptibility, χT , of NiTTFt also has a weak temperature-dependence which may be attributed to a paramagnetic contribution from charge carriers, namely Pauli paramagnetism (Fig. 2b). There is also a deviation from linearity in χT at low temperatures which we note coincides with the above discussed increase in resistivity and putative localization. Regardless, the value of χ_{Pauli} , $6 \times 10^{-4} \text{ cm}^3/\text{mol}$, is consistent with reported values in organic metals.^{7,8}

The combined data on NiTTFt supports its assignment as a glassy metal, but we wanted to obtain more detailed quantification of its metallic nature and so we used both diffuse and specular reflectance spectroscopies (Fig. 2e).^{30, 31} NiTTFt has a broad absorption over the UV-vis-NIR region up to $\sim 12000 \text{ cm}^{-1}$. At the low frequency limit, the Hagen-Rubens relation can be used to extrapolate the specular reflectance to zero frequency and thereby estimate the optical dc conductivity as $\sim 4200 \text{ S/cm}$, a value which is consistent with four-probe conductivity of pressed pellets (1280 S/cm). The observed plasma frequency of $\sim 12,000 \text{ cm}^{-1}$ suggests a carrier density of 10^{21} cm^{-3} which is similar to values in crystalline metallic polymers.^{1,26} Crude Hall effect measurements support this value ($5 \times 10^{21} \text{ cm}^{-3}$, Fig. S29).

We have further analyzed the reflectivity data by applying the Kramers-Kronig (KK) transformation (Fig. 2f). Surprisingly, the optical conductivity from this analysis continuously increases as the frequency goes to zero. This behavior, particularly in the far-IR region below 3000 cm^{-1} , is suggestive of Drude behavior for a classic metal.³² While the data range and quality limit fitting reliability, we have nonetheless analyzed this data with a Drude model ($\sigma D(\omega) = (\omega_p^2 \tau / 4\pi)(1 + \omega^2 \tau^2)^{-1}$) which gives a plasma frequency of about $12,100 \text{ cm}^{-1}$, a relaxation time of $9.0 \times 10^{-15} \text{ s}$, a dc conductivity of $\sim 3300 \text{ S/cm}$, and a carrier density of $3 \times 10^{21} \text{ cm}^{-3}$ (assuming $m^* = 2m_e$). All fitted and measured values for NiTTFt across different techniques are consistent with each other and again support metallic behavior. The Drude-like behavior and small T_{ES} values furthermore raise the possibility of band-like ballistic charge transport limited by hopping across macroscopic grain boundaries.

Amorphous organic conducting polymers also exhibit high conductivity, but the mechanism of charge transport in these materials is typically not metallic or intrinsic and relies upon doped

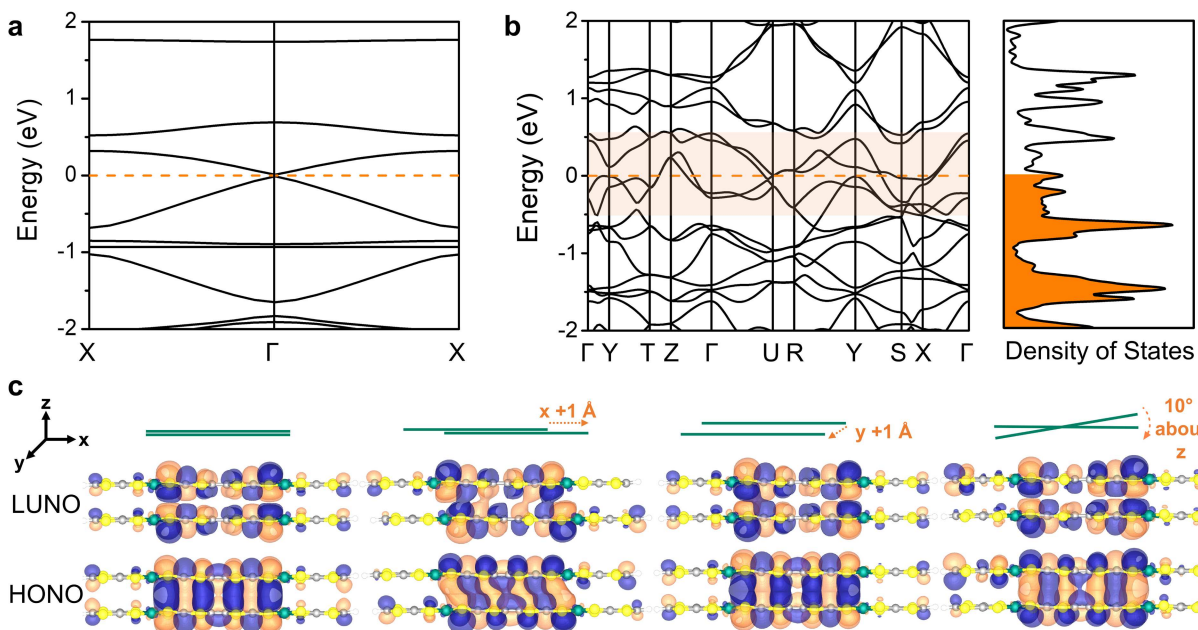


Fig. 3 Theoretical analysis of NiTTFt. **a**, Computed band structure of an isolated chain. **b**, Computed band structure of the idealized 3D structure determined from experimental data. **c**, Orbital diagrams of a molecular dimer of NiTTFt building blocks showing that significant overlap is maintained regardless of structural distortions.

charge carriers.⁶ In intrinsic organic conductors, metallic character is always accompanied by crystalline order. The properties of NiTTFt, which exhibits intrinsic metallic charge transport with a fundamentally disordered structure, are thus highly unusual. We have therefore undertaken detailed theoretical analyses of NiTTFt to better understand this apparent dichotomy.

Theoretical Analysis

Density functional theory calculations were undertaken on 1D chains and 3D stacks of NiTTFt based on our structural model. Interestingly, isolated 1D chains of NiTTFt show semi-metallic behavior but exhibit a metallic band structure upon 3D assembly (Fig. 3a and b respectively). Analysis of the band structure shows that metallic character arises from both π -stacking interactions within the 2D sheets (Γ to Z), as well as side-to-side S–S interactions between sheets which broaden the bands near the Fermi level (Γ to X). Similar interactions have been invoked in single-component molecular conductors.⁷ In addition to these periodic calculations, we have also analyzed why the metallic character of NiTTFt is maintained with disorder by examining molecular models which can be systematically distorted (Fig. 3c). Two molecular fragments of NiTTFt were fixed at positions which vary the slip, π -stacking, and side-to-side distances as well as the interchain twist angle. The electronic structures of these models were analyzed by variational 2-electron reduced density matrix (V2RDM) complete active space self-consistent field (CASSCF) calculations.³³ This analysis demonstrates that the molecular fragments of NiTTFt have significant overlap and correlation that is remarkably robust to disorder. This is perhaps best illustrated by the fact that the HONO-LUNO gaps have little to no change with structural distortions (Table S4). These computations explain how metallic character is preserved in amorphous NiTTFt: periodicity is disrupted by small scale structural disorder, but these defects are not significant enough to disrupt overlap, correlation, and delocalization.

Thermal and Aerobic Stability

The combination of structural disorder and intrinsic metallic character in NiTTFtt suggests some advantageous properties. Organic conductors, including n-type conducting polymers,³⁴ metallic coordination polymers like Cu₃BHT, and molecular conductors, typically suffer from fast degradation when exposed to air and heat.²⁶ Metallic character in these systems arises from their crystalline structure which can be disrupted with sufficient thermal energy (i.e. melting or decomposition), and exposure to air and heat leads to chemical reactions that remove charge carriers and reduce conductivity.⁹ While these are significant issues in applications of conducting organic materials, the disordered structure and intrinsic electronic properties of NiTTFtt suggest that this material should be significantly more robust.

Thermogravimetric analysis shows that NiTTFtt exhibits good stability both under N₂ gas (up to 270 °C) but also, remarkably, in air (up to 235 °C, Fig. 4a). Inspired by the stability of NiTTFtt, we monitored sheet resistance (R_{sheet}) in air while heating and cooling between 20 and 140 °C (Fig. 4b). The data clearly show that the high electrical conductivity of NiTTFtt is preserved even under these comparatively harsh conditions. The same sample was left in air over a month with no conductivity loss (Fig. 4c). These data demonstrate that the unusual combination of intrinsic metallic character with an amorphous structure in NiTTFtt imparts substantial stability for conductivity with heat and air.

Conclusion

Organic conductors are an enormously important class of materials. To realize conductivity in normally insulating organic materials it is typically necessary to optimize their electronic structure through doping and their geometric structure through crystallinity. However, the requirement for doping and crystallinity imposes restrictions on composition and stability. Here we report an unusual new material, NiTTFtt, that is structurally amorphous, precluding a classical band structure. Nevertheless, detailed characterization of NiTTFtt reveals high conductivity and metallic character. Theory shows that the presence of this metallic behavior is enabled by significant overlap between the molecular units of NiTTFtt that is insensitive to structural distortions. The exact mechanism of charge transport at the limit of no structural ordering is still unclear, with data raising the possibility of both hopping and band-like transport. Similar questions

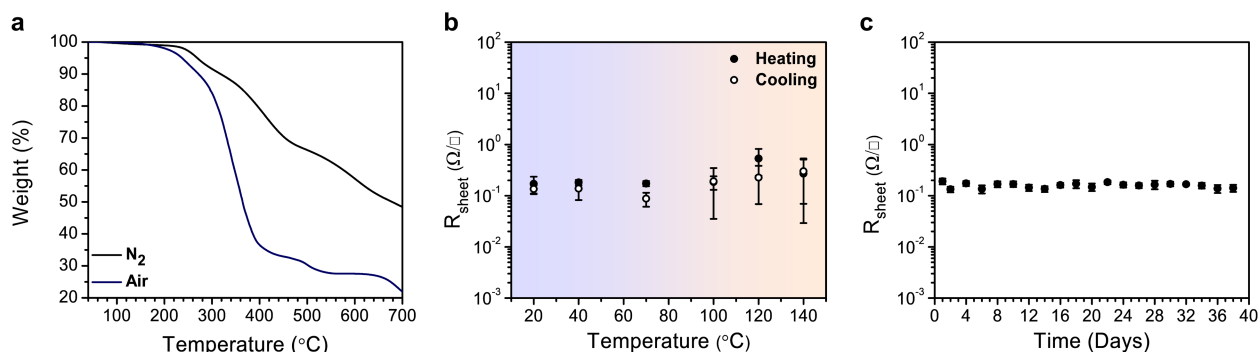


Fig. 4 Thermal and aerobic stability of NiTTFtt. **a**, Thermogravimetric analysis under N₂ and air. **b**, Sheet resistance in air upon heating and cooling. **c**, Long-term stability of the resistance in air.

have been discussed in all-inorganic glassy metals, and NiTTFtt shows that the same interesting phenomena are present in organic materials composed of significantly more complex and tunable molecular building blocks. Regardless, the juxtaposition of metallic character and disorder in NiTTFtt provides remarkable thermally and aerobically stable conductivity. These results demonstrate that the use of molecular units that have strong overlap, and subsequently strong electronic delocalization, can lead to metallic character even in completely amorphous materials.

Methods

Synthesis

Unless otherwise noted, all synthetic manipulations were performed under an inert atmosphere of dry N₂ using a Schlenk line or a N₂-filled MBraun UNILab glovebox. Dichloromethane (DCM) was initially dried and sparged with Ar on a solvent purification system from Pure Process Technologies and stored over 4 Å molecular sieves. Methanol (MeOH) was dried with NaOH and distilled before being transferred into the glovebox. The dried MeOH was then passed through activated alumina and stored over 4 Å molecular sieves in the glovebox. TTFtt(SnBu₂)₂ (TTFtt = tetrathiafulvalene-2,3,6,7-tetrathiolate; Bu=n-butyl), Fc^{BzO}BAR^F₄ (Fc^{BzO} = benzoyl ferrocenium; [BAR^F₄] = tetrakis(3,5-bis(trifluoromethyl)phenyl)borate), and [TEA]₂[NiCl₄] (TEA = tetraethylammonium) were synthesized following previously reported procedures.^{15, 35}

NiTTFtt TTFtt(SnBu₂)₂ (0.667 mmol, 266 mg) in 5 mL DCM was mixed with Fc^{BzO}BAR^F₄ (1.33 mmol, 1.54 g) in 5 mL DCM resulting in a homogenous dark purple solution. The resulting solution was added into a 10 mL MeOH solution of [TEA]₂[NiCl₄] (2.00 mmol, 920 mg) with vigorous stirring. The mixture was kept stirring at 40 °C overnight. The solid product was isolated via centrifugation and washing with DCM (3×12 mL), MeOH (1×12 mL) and DCM (1×12 mL) sequentially. After being dried under vacuum at 100 °C overnight, 235 mg of NiTTFtt was isolated as a black powder (91%).

Semicrystalline NiTTFtt TTFtt(SnBu₂)₂ (0.040 mmol, 43 mg) in 0.4 mL DCM was mixed with Fc^{BzO}BAR^F₄ (0.080 mmol, 93 mg) in 0.4 mL DCM to form a homogenous dark purple solution. After mixing, 0.8 mL of this dark purple solution was added into a clean 5 mL shell vial and 2.4 mL of a 1:1 DCM:MeOH solution (by volume) and then 0.8 mL of pure MeOH were slowly layered on the DCM layer sequentially, forming three distinct layers. Finally, a 0.8 mL MeOH solution of [TEA]₂[NiCl₄] (0.12 mmol, 55 mg) was layered on top. The shell vial was carefully capped and placed in a secondary 24 mL vial which was allowed to sit and diffuse for 5 days. The resulting black powders were collected and washed identically to the procedure for amorphous NiTTFtt described above yielding 13 mg (85%).

Pressed pellets were prepared at 800 MPa in the glovebox by using a hydraulic pellet press (TMAX-15T) and dies with different sizes (7, 8, and 12 mm round dies and 6 mm square dies). Hot pressing was carried out with an additional heated die (13 mm Across International heated die with digital controller). Prior to pressing, powders were ground to particle sizes below 20 μm. For hot pressed samples, 240 mg of powder was ground with a ball mill (Spex SamplePrep 5100 Mixer miller, 440C steel balls) for 15 mins (in air) and loaded into 13 mm round dies that were preheated to 200 °C (under N₂). During pressing the pressure was maintained for 20 mins after stabilizing at 800 MPa. The thickness of the pressed pellets is around 100-300 μm.

Structural Characterization

X-ray Powder Diffraction (PXRD) for screening reaction conditions were performed on a SAXSLAB Ganesha equipped with a Xenocs GeniX3D Cu K α source. Samples were loaded into 0.8–1.1 mm ID, 0.25 mm wall borosilicate capillaries and sealed with wax. Data reduction/integration was performed using the Saxsgui software and a background correction for the capillary was applied. Additionally, both amorphous and semicrystalline NiTTFtt samples were analyzed with a long-collection (24h) absorption measurement on a Rigaku SmartLab X-ray diffractometer equipped with a HyPix3000 detector. Both samples of amorphous and semicrystalline NiTTFtt were loaded into 1.0 mm OD, 0.01 mm wall borosilicate capillaries as fine powders and sealed with wax. All measurements were carried out with a Cu K α radiation (1.54186 Å) in a transmission mode. Scans were measured using a parallel beam mode selected through the attached Cross Beam Optics. The tube was energized at 44 mA and 40 kV. The data collections were completed in SmartLab Studio II software package (version 4.4.241.0).

Synchrotron X-ray Powder Diffraction was collected at beamline 11-BM at the Advanced Photon Source at Argonne National Laboratory (Lemont, IL, USA). The sample of semicrystalline NiTTFtt was loaded into Cole-Parmer Polyimide tubing provided by the beamline and capped with clay. The powders were rotated during the measurement at ~50 Hz. The powder patterns were measured at 295 K using a wavelength of $\lambda = 0.458126$ Å, from 0.5 to 50° 2 θ with a step size of 0.001° and a counting time of 0.1 s/step.

X-ray Absorption Spectroscopy Powder samples of amorphous NiTTFtt were prepared by grinding finely with polypropylene as a binder. A Teflon washer (5.3 mm internal diameter) was sealed on one side with Kapton tape and the ground powder was then transferred to the inside of this ring before compacting with a Teflon rod and sealing the remaining face with Kapton tape. X-ray absorption near-edge spectra (XANES) of Ni K-edge (8333 eV) data were acquired at the MRCAT 10-BM beam line in transmission at the Advanced Photon Source at Argonne National Laboratory with a bending magnet source with ring energy at 7.00 GeV. Data collected was processed using the Demeter software suite³⁶ by extracting the EXAFS oscillations $\chi(k)$ as a function of photoelectron wavenumber k . The theoretical paths were generated using FEFF6³⁷ and the models were done in the conventional way using the fitting program Artemis.

X-ray Total Scattering and Pair Distribution Function Analysis Samples of semicrystalline and amorphous NiTTFtt were loaded into Cole-Parmer Polyimide tubing provided by the beamline and capped with clay. High-energy X-ray total scattering experiments were performed at 11-ID-B at the Advanced Photon Source, with an X-ray wavelength of 0.2115 Å. The raw 2D data were azimuthally integrated and reduced to 1D intensity *versus* 2 θ in GSAS-II³⁸ using CeO₂ powder for the calibration to determine sample to detector distance. PDFgetX2 program³⁹ was used to correct and normalize the diffraction data and then Fourier transform the reduced structure factor to obtain the PDF, $G(r)$.

Scanning Electron Microscope (SEM) images were taken on a Carl Zeiss Merlin using the In-Lens detector in the Materials Research Science and Engineering Center (MRSEC) at the University of Chicago. The accelerating voltage is 5.00 kV.

Composition and Vibrational Characterization

X-ray Photoelectron Spectra (XPS) were collected with the AXIS Nova spectrometer (Kratos Analytical) equipped with a monochromatic Al K α X-ray source. The Al anode was powered at 10 mA and 15 kV. The instrument work function was calibrated to give a Au 4f $_{7/2}$ metallic gold binding energy of 83.95 eV. The instrument base pressure was ca. 1×10^{-10} Torr. The analysis area size was 0.3×0.7 mm 2 . For calibration purposes, the binding energies were referenced to the C 1s peak at 284.8 eV. Survey spectra were collected with a step size of 1 and 160 eV pass energy.

Ultraviolet Photoelectron Spectra (UPS) were collected with the AXIS Nova spectrometer using UV-radiation source. The high-resolution spectra were collected with a pass energy of 40 and a 0.1 eV step size. 7 mm cold pressed pellets were affixed to conductive carbon tape under N $_2$ before loading into the spectrometer.

Inductively Coupled Plasma (ICP) ICP-mass spectrometry (ICP-MS) data was obtained with an Agilent 7700x ICP-MS and analyzed using Mass Hunter version B01.03. Solutions for ICP-MS were prepared by digesting 2 mg of material in 1 mL HNO $_3$ (trace metal grade) solution in a fume hood overnight and diluted with ultrafiltered deionized water. An Agilent 700 series spectrometer was used for ICP-optical emission spectroscopy (ICP-OES). The sample preparation was referred to the reported procedure⁴⁰ to improve the accuracy of Sulfur determination. Solutions for ICP-OES were prepared by digesting 2 mg of materials in 0.5 mL HNO $_3$ and 0.5 mL H $_2$ O $_2$ (trace metal grade) solutions in tight-sealed high-density polyethylene (HDPE) centrifuge tubes overnight and then diluted with ultrafiltered deionized water.

X-ray Fluorescence (XRF) measurements were performed on pressed pellets with a Rigaku NEX DE VS spectrometer under a He atmosphere.

Combustion Elemental Analyses (C, H, N) were performed by Midwest Microlabs.

Electron Paramagnetic Resonance (EPR) spectra were recorded on a Bruker Elexsys E500 spectrometer with an Oxford ESR 900 X-band cryostat and a Bruker Cold-Edge Stinger. NiTTfTt was mixed and ground with dry KBr powder into a uniform mixture (concentration is ~ 0.5 mg/1g KBr). This “solid matrix” was loaded into the EPR tube to fill about 0.1 mL volume.

Infrared Spectra were recorded on a Bruker Tensor II FTIR spectrometer with MCT detector operated at 77 K. Data were processed and background corrected with OPUS software (version 7.5). Samples were prepared under N $_2$ by grinding solid sample with dry KBr powder, pressed as pellets, and measured in air under ambient conditions.

Raman Spectra were obtained with a Horiba LabRamHR Evolution confocal microscope. A Si (111) wafer was used for calibration. The sample of a 7 mm round pressed pellet of NiTTfTt powder was excited using a 532 nm light source operating at 5 % of its power and using 100x long path objective and a 600 mm $^{-1}$ grating.

Physical Characterization

Room-Temperature Electrical Conductivity and Seebeck Measurements are based on a previously reported setup.⁴¹ Gold electrical contacts (75 nm thick) were deposited onto 8 mm pressed pellets via thermal evaporation through homemade shadow masks. Four probe

conductivity measurements were performed using a custom-designed probe station in an argon-filled glovebox. Voltage and current measurements were performed using a Keithley 2400 source meter and a Keithley 6221 precision current source. The Seebeck coefficient measurements were performed on the same probe station. Two Peltier elements were placed 5 mm apart to provide the temperature difference ($\Delta T = T_H - T_C$). Two thermocouples were used to collect the hot and cold side temperatures, and two probes were used to measure the corresponding voltage value. A minimal amount of thermally conductive silicone paste was applied to the tips of the thermocouple to ensure good thermal contact between the thermocouple and the gold pads. A delay of 200 s was used for voltage measurements to ensure that a steady-state temperature gradient and voltage were reached. The Seebeck coefficient was calculated from the slope of a linear fit for the ΔV vs ΔT plot. The measurements were taken within an approximate ΔT of ± 3 K around 300 K.

Thermal Conductivities of the samples were determined through single-laser Raman thermometry using the same Confocal Raman Microscope discussed above based on a reported method.²² In Raman thermometry, a focused laser beam is used as a heat source, while the temperature-dependent Raman spectra are used as a thermometer. First, the spectral positions of the Raman peaks around 495 cm^{-1} were measured as a function of the incident absorbed laser power ($\lambda = 532 \text{ nm}$). The laser power was varied by using 0.1, 1, 2.5, and 5% of the max power of the 532 nm light source. The individual powers were examined with a Si power detector. The operational setup also includes a 100x long path objective and an 1800 mm^{-1} grating. Secondly, the shift in the spectral position of the Raman peaks is recorded as a function of temperature, which is controlled externally by a Linkam cryostat in air.

The temperature rise in the laser spot region for the case of a semi-infinite medium can be written as:

$$\Delta T = \frac{P_{abs}}{\pi R k}$$

where P_{abs} is the laser power absorbed by the sample, R is the Gaussian spot radius, and k is the thermal conductivity of the specimen. R is calculated by using and the ToptiCalcTM program and based on the technical information of the laser source and the lens.

Variable-Temperature Electrical Resistance A strip of double-sided polyimide tape was placed on a DC Resistivity/ETO Sample Puck (Quantum Design P102), which serves as an electrical insulator, and then pressed pellets with 75 nm thick deposited gold contacts were put on the top of the tape. Then 0.015 inch-OD Indium wires were used to bond to the samples' gold nodes as shown in Fig. S24. The puck was then loaded into a physical property measurement system (PPMS, Quantum Design) under a He-filled inert atmosphere. The 4-point probe resistivity measurements on a 13 mm hot pressed pellet and 2-point probe resistivity measurements on 8 mm cold pressed pellets were carried out in an AC mode with a DC excitation of 1 mA. The temperature dependent resistivity/resistance measurements were performed from 300 K to 2 K.

Variable-Temperature Seebeck Coefficients were measured with MMR Technologies Inc. K-20 Programmable Temperature Controller and P-100 Programmable Seebeck Controller. A 1 mm \times 4 mm piece of a pressed pellet was gently put between electrodes of the sample chip. Ag epoxy (Epoxy Technology H20E) was used for the connection between the sample and the electrodes. The sample chip was heated in a muffle furnace at 175 °C for 0.5 h for a complete curing, before loading the chip into the sample device. The whole preparation was finished in air. Temperature-

dependent Seebeck measurements were performed from 300 to 400 K and Seebeck measurements at each temperature repeated three times.

Solid-State Magnetic Measurements were performed on a Quantum Design MPMS3 SQUID magnetometer. The bulk powder of the sample (36.0 mg) was suspended in an eicosane matrix in a polycarbonate capsule to prevent movement. Diamagnetic corrections for the capsule and eicosane were made by measuring temperature vs moment in triplicate for each to determine a moment per gram correction. Diamagnetic corrections for the sample itself were applied using Pascal's constants of each atom based on the formula of NiC_6S_8 .

Hall Effect Measurements A 6×6 mm squared pressed pellet (264 μm) and a double-sided polyimide tape was put on the Sample Puck (P102). By using fast-drying Ag paint (Ted Pella 16040-30) and Indium wires, the device was set up as shown in Fig. S28. The Hall effect experiments were carried out on PPMS at 300 K. The max current, 5 mA was used during the test. While the magnetic field was scanned between 0-7 T, R_{xy} (V_{hall}/I) the Hall coefficient ($R_H = dR_{xy}/dH$) was calculated based on the linear fit.

UV-Vis-NIR Diffuse Reflectance Spectra were collected on a Varian Cary 5000 spectrophotometer with powder samples loaded in a Praying Mantis air-free diffuse reflectance cell with KCl powder as the non-adsorbing matrix. The Kubelka-Munk conversion of the raw diffuse reflectance spectrum was obtained by applying the formula $F(R) = (1-R)^2/2R$.

UV-Vis-NIR Specular Reflectance Spectra (200-2000 nm) were collected on Shimadzu UV-3600 Plus UV-VIS-NIR spectrophotometer with a 5-degree relative specular reflectance accessory. IR specular reflectance spectra ($570\text{-}8000\text{ cm}^{-1}$) were collected with 64 scans at a spectral resolution of 4 cm^{-1} on an IR microscope (Hyperion 2000, Bruker Optics Inc., USA) coupled to a Fourier transform infrared (FTIR) spectrometer (Vertex 70, Bruker Optics Inc., USA) with a mid-IR glowbar source. Since the rough surface of the pressed pellet causes non-specular reflectance light loss compared to mirror standards, the experiments were conducted following a reported method³¹ based on pressed pellets with a metal-coating. First, a 12 mm pressed pellet of NiTTFtt was coated with 100 nm thick aluminum covering a half of one face and on the other face, 100 nm thick gold was applied in the same way. Second, for UV-NIR reflectance spectra, we measured the relative reflectance of both the sample surface and aluminum-coated surface, separately with respect to the aluminum mirror. Finally, the absolute reflectance spectrum of NiTTFtt was obtained by dividing the sample's reflectance with that of the aluminum-coated surface. For the IR spectrum, the method is similar but instead of aluminum, gold was used as the reference.

Stability Tests

Thermogravimetric Analysis (TGA) was performed using a TA Instruments Discovery analyzer. Approximately 2 mg of sample was loaded into a pre-tared Pt pan and measured under N_2 or air. Samples were measured from 35 $^\circ\text{C}$ to 700 $^\circ\text{C}$ using a linear temperature ramp of 10 $^\circ\text{C min}^{-1}$. The decomposition temperature was defined by the one where less than 95% mass is left.

High Temperature Variable-Temperature Resistance A 7 mm pressed pellet (thickness, 162 μm) was symmetrically deposited with four gold nodes on the edges. The heated resistance measurements were carried out in air with a home-made setup as shown in Fig. S34. A polyimide

flexible heater (PLM-106/10-P) was used as the heat source, whose temperature was read and controlled by a temperature controller (Digi-Sense Advanced Temperature Controller, Cole Parmer). The sample temperature was read by a thermometer (Traceable Thermocouple). The sheet resistances were measured by Semiconductor Device Analyzer (Keysight B1500A) with the van der Pauw method.

Long-Term In-Air Resistance Measurements After the high temperature varied-temperature resistance measurements were done, the same setup and the sample were maintained in air and the resistance at room temperature was examined every 2 days.

Theoretical Calculations

Band Structure Calculations In these calculations, we determine the band structure and density of states for the 3D dimer, 3D monomer, and 1D monomer models using Density Functional Theory (DFT) in Quantum espresso.^{42, 43} The kinetic energy cutoff of basis plane-wave functions (100 Ry), Marzari-Vanderbilt-DeVita-Payne cold smearing⁴⁴ temperature (0.001 Ry), energy convergence threshold (1e-8 Ry), and k-point sampling were optimized to reduce error in the band structure. All calculations used a PAW pseudopotential with a PBE functional and a nonlinear core correction from PSLibrary.^{45, 46} Brillouin zones are generated by the SeeK-path tool,^{47, 48} and only relevant points used in the band structure of the primitive cell were included for clarity.

Molecular Calculations A bimolecular model was constructed from the NiTTFtt solid structure to emulate the inter-layer interactions present in the amorphous extended structure, with the individual unit displayed in Fig. 3c. An inter-layer distance of 3.35Å was chosen based on the average distance in the proposed structure. The results for B3LYP⁴⁹/6-31G*⁵⁰ with the GD3BJ⁵¹ dispersion correction and [20,20] active space variational 2-electron reduced density matrix (V2RDM)³³/6-31G⁵² calculations are displayed in Table S4. To further understand the energetics of the inter-unit displacements, CASSCF calculations were carried out with the V2RDM method and a large active space of 20 electrons distributed in 20 molecular orbitals ([20,20]) with a 6-31G basis set.

References

- ¹ Heeger, A. J. Nobel Lecture: Semiconducting and metallic polymers: The fourth generation of polymeric materials. *Rev. Mod. Phys.* **73**, 681–700 (2001).
- ² Bryce, M. R. Recent progress on conducting organic charge-transfer salts. *Chem. Soc. Rev.* **20**, 355 (1991).
- ³ Valade, L., de Caro, D., Faulmann, C. & Jacob, K. TTF[Ni(dmit)₂]₂: From single-crystals to thin layers, nanowires, and nanoparticles. *Coord. Chem. Rev.* **308**, 433–444 (2016).
- ⁴ Xie, L. S., Skorupskii, G. & Dincă, M. Electrically conductive metal–organic frameworks. *Chem. Rev.* **120**, 8536–8580 (2020).
- ⁵ Guo, X. & Facchetti, A. The journey of conducting polymers from discovery to application. *Nat. Mater.* **19**, 922–928 (2020).
- ⁶ Bubnova, O. *et al.* Semi-metallic polymers. *Nat. Mater.* **13**, 190–194 (2014).
- ⁷ Kobayashi, A., Fujiwara, E. & Kobayashi, H. Single-Component Molecular Metals with Extended-TTF Dithiolate Ligands. *Chem. Rev.* **104**, 5243–5264, (2004).
- ⁸ Kobayashi, Y., Terauchi, T., Sumi, S. & Matsushita, Y. Carrier generation and electronic properties of a single-component pure organic metal. *Nat. Mater.* **16**, 109–114 (2017).

- ⁹ Venkateshvaran, D. *et al.* Approaching disorder-free transport in high-mobility conjugated polymers. *Nature* **515**, 384–388 (2014).
- ¹⁰ Joo, Y., Agarkar, V., Sung, S. H., Savoie, B. M. & Boudouris, B. W. A nonconjugated radical polymer glass with high electrical conductivity. *Science* **359**, 1391–1395 (2018).
- ¹¹ Plummer, J. Is metallic glass poised to come of age? *Nat. Mater.* **14**, 553–555 (2015).
- ¹² Hirata, A. *et al.* Geometric frustration of icosahedron in metallic glasses. *Science* **341**, 376–379 (2013).
- ¹³ Eisenberg, R. & Gray, H. B. Noninnocence in metal complexes: A dithiolene dawn. *Inorg. Chem.* **50**, 9741–9751 (2011).
- ¹⁴ McCullough, R. D. *et al.* Building block ligands for new molecular conductors: homobimetallic tetrathiafulvalene tetrathiolates and metal diselenolenes and ditellurolenes. *J. Mater. Chem.* **5**, 1581 (1995).
- ¹⁵ Xie, J. *et al.* Redox, transmetalation, and stacking properties of tetrathiafulvalene-2,3,6,7-tetrathiolate bridged tin, nickel, and palladium compounds. *Chem. Sci.* **11**, 1066–1078 (2020).
- ¹⁶ de Caro, D. *et al.* Metallic Thin films of TTF[Ni(dmit)₂]₂ by electrodeposition on (001)-oriented silicon substrates. *Adv. Mater.* **16**, 835–838 (2004).
- ¹⁷ Scott, R. A. Comparative X-ray absorption spectroscopic structural characterization of nickel metalloenzyme active sites. *Phys. B Condens. Matter* **158**, 84–86 (1989).
- ¹⁸ Holder, C. F. & Schaak, R. E. Tutorial on powder X-ray diffraction for characterizing nanoscale materials. *ACS Nano* **13**, 7359–7365 (2019).
- ¹⁹ Tanaka, H., Okano, Y., Kobayashi, H., Suzuki, W. & Kobayashi, A. A three-dimensional synthetic metallic crystal composed of single-component molecules. *Science* **291**, 285–287 (2001).
- ²⁰ Vogt, T. *et al.* A LAXS (large angle X-ray scattering) and EXAFS (extended X-ray absorption fine structure) investigation of conductive amorphous Nickel tetrathiolato polymers. *J. Am. Chem. Soc.* **110**, 1833–1840 (1988).
- ²¹ Huang, X. *et al.* Superconductivity in a Copper(II)-based coordination polymer with perfect Kagome structure. *Angew. Chemie Int. Ed.* **57**, 146–150 (2018).
- ²² Liu, Z. *et al.* Controlling the Thermoelectric properties of organometallic coordination polymers via ligand design. *Adv. Funct. Mater.* **30**, 2003106 (2020).
- ²³ Xiang, L., Ji-hua, G. & Jun-hao, C. Thermal conductivity of metallic wires. *Chinese Phys.* **10**, 223–228 (2001).
- ²⁴ Sun, L. *et al.* A microporous and naturally nanostructured thermoelectric metal-organic framework with ultralow thermal conductivity. *Joule* **1**, 168–177 (2017).
- ²⁵ Dou, J. H. *et al.* Signature of metallic behavior in the metal-organic frameworks M₃(hexaiminobenzene)₂ (M = Ni, Cu). *J. Am. Chem. Soc.* **139**, 13608–13611 (2017).
- ²⁶ Kaiser, A. B. Electronic transport properties of conducting polymers and carbon nanotubes. *Reports Prog. Phys.* **64**, 1–49 (2001).
- ²⁷ Halim, J. *et al.* Variable range hopping and thermally activated transport in molybdenum-based MXenes. *Phys. Rev. B* **98**, 104202 (2018).
- ²⁸ Lan, X. *et al.* Quantum dot solids showing state-resolved band-like transport. *Nat. Mater.* **19**, 323–329 (2020).
- ²⁹ Kang, S. D.; Dylla, M.; Snyder, G. J. Thermopower-conductivity relation for distinguishing transport mechanisms: polaron hopping in CeO₂ and band conduction in SrTiO₃. *Phys. Rev. B* **97**, 235201 (2018).
- ³⁰ Heeger, A. J. Disorder-induced metal-insulator transition in conducting polymers. *J. Supercond.* **14**, 261–268 (2001).

- ³¹ Jiang, Y. *et al.* Synthesis of a Copper 1,3,5-triamino-2,4,6-benzenetriol metal–organic framework. *J. Am. Chem. Soc.* **142**, 18346–18354 (2020).
- ³² Lee, K. *et al.* Metallic transport in polyaniline. *Nature* **441**, 65–68 (2006).
- ³³ Mazziotti, D. A. Large-scale demidefinite programming for many-electron quantum mechanics. *Phys. Rev. Lett.* **106**, 083001 (2011).
- ³⁴ He, T., Stolte, M. & Würthner, F. Air-stable n-channel organic single crystal field-effect transistors based on microribbons of core-chlorinated naphthalene diimide. *Adv. Mater.* **25**, 6951–6955 (2013).

Acknowledgement

This work was supported by the Army Research Office under Grant W911NF-20-1-0091. DAM and JSA thank support from the U.S. Department of Energy, Office of Science, Office of Basic Energy Sciences, under Award DE-SC0019215. We thank Nicholas Boynton and Ben Ketter for assistance with Seebeck measurements, Daniel Laorenza and Prof. Danna Freedman for assistance with diffuse reflectance spectroscopy, Xiaomin Jiang, Yingjie Fan, Taokun Luo and Prof. Wenbin Lin for assistance with ICP-MS measurements and Jia-Ahn Pan for assistance with ICP-OES measurements. We thank Andrew Ritchhart for the structure's geometry optimization and Lei Wang for SEM. This research used resources of the Advanced Photon Source (APS), a U.S. Department of Energy (DOE) Office of Science User Facility operated for the DOE Office of Science by Argonne National Laboratory under Contract No. DE-AC02-06CH11357. We thank McKenna Goetz and beamline staff, Yujia Ding and Kamil Kucuk, for assistance with XAS measurements at beamline APS 10-BM-A, B and Leighanne C. Gallington for X-ray total scattering measurements at beamline APS 11-ID-B. Parts of this work were carried out at the Soft Matter Characterization Facility of the University of Chicago. This work made use of the shared facilities at the University of Chicago Materials Research Science and Engineering Center, supported by National Science Foundation under award number DMR-2011854. This research is based upon work supported by the National Science Foundation under Grant No. NSF CHE-1856684.

Author Contribution

J.Z. synthesized samples and performed the physical characterizations. S.E. conducted band structure calculations and J-N.B. performed the molecular calculations. B.C. performed electrical measurements and gold depositions. A. S. F performed and refined the structural determination. T.M. carried out the room temperature Seebeck and four-probe conductivity measurements. N.Z. and R.I. collected Raman and specular reflectance IR spectra, respectively. X.S. performed the KK analysis. H.C. measured variable-temperature Seebeck coefficients. J.X. and J.S.A. conceived and wrote the manuscript. B.C., S.N.P., D.V.T., J.P., and D.A.M interpreted the data and wrote the manuscript.

³⁵ Gill, N. S. & Nyholm, R. S. 802. Complex halides of the transition metals. Part I. Tetrahedral nickel complexes. *J. Chem. Soc.* 3997 (1959).

³⁶ Ravel, B. & Newville, M. ATHENA, ARTEMIS, HEPHAESTUS: data analysis for X-ray absorption spectroscopy using IFEFFIT. *J. Synchrotron Radiat.* **12**, 537–541 (2005).

- ³⁷ Rehr, J. J. & Albers, R. C. Theoretical approaches to X-ray absorption fine structure. *Rev. Mod. Phys.* **72**, 621–654 (2000).
- ³⁸ Toby, B. H. & Von Dreele, R. B. GSAS-II: the genesis of a modern open-source all purpose crystallography software package. *J. Appl. Crystallogr.* **46**, 544–549 (2013).
- ³⁹ Qiu, X., Thompson, J. W. & Billinge, S. J. L. PDFgetX2: a GUI-driven program to obtain the pair distribution function from X-ray powder diffraction data. *J. Appl. Crystallogr.* **37**, 678–678 (2004).
- ⁴⁰ Morrison, C., Sun, H., Yao, Y., Loomis, R. A. & Buhro, W. E. Methods for the ICP-OES analysis of semiconductor materials. *Chem. Mater.* **32**, 1760–1768 (2020).
- ⁴¹ Ma, T., Dong, B. X., Grocke, G. L., Strzalka, J. & Patel, S. N. Leveraging sequential doping of semiconducting polymers to enable functionally graded materials for organic thermoelectrics. *Macromolecules* **53**, 2882–2892 (2020).
- ⁴² Giannozzi, P. *et al.* QUANTUM ESPRESSO: a modular and open-source software project for quantum simulations of materials. *J. Phys. Condens. Matter* **21**, 395502 (2009).
- ⁴³ Giannozzi, P. *et al.* Advanced capabilities for materials modelling with Quantum ESPRESSO. *J. Phys. Condens. Matter* **29**, 465901 (2017).
- ⁴⁴ Marzari, N., Vanderbilt, D., De Vita, A. & Payne, M. C. Thermal contraction and disordering of the Al(110) Surface. *Phys. Rev. Lett.* **82**, 3296–3299 (1999).
- ⁴⁵ Prandini, G., Marrazzo, A., Castelli, I. E., Mounet, N. & Marzari, N. Precision and efficiency in solid-state pseudopotential calculations. *npj Comput. Mater.* **4**, 72 (2018).
- ⁴⁶ Lejaeghere, K. *et al.* Reproducibility in density functional theory calculations of solids. *Science*. **351**, (2016).
- ⁴⁷ Hinuma, Y., Pizzi, G., Kumagai, Y., Oba, F. & Tanaka, I. Band structure diagram paths based on crystallography. *Comput. Mater. Sci.* **128**, 140–184 (2017).
- ⁴⁸ Togo, A. & Tanaka, I. Spglib: a software library for crystal symmetry search. 1–11 (2018).
- ⁴⁹ Becke D., A. Density-functional thermochemistry. III. The role of exact exchange. *The Journal of Chemical Physics* vol. 98 5648–5652 (1993).
- ⁵⁰ Francl, M. M. *et al.* Self-consistent molecular orbital methods. XXIII. A polarization-type basis set for second-row elements. *J. Chem. Phys.* **77**, 3654–3665 (1982).
- ⁵¹ Grimme, S., Ehrlich, S. & Goerigk, L. Effect of the damping function in dispersion corrected density functional theory. *J. Comput. Chem.* **32**, 1456–1465 (2011).
- ⁵² Hehre, W. J., Ditchfield, R. & Pople, J. A. Self-consistent molecular orbital methods. XII. further extensions of Gaussian-type basis sets for use in molecular orbital studies of organic molecules. *J. Chem. Phys.* **56**, 2257–2261 (1972).

Supplementary Files

This is a list of supplementary files associated with this preprint. Click to download.

- [SupplementaryInformation.pdf](#)